AGU PUBLICATIONS

JGR

Journal of Geophysical Research: Space Physics

RESEARCH ARTICLE

10.1002/2015JA022057

Key Points:

- SAPS-WS impacted more intensively stagnation trough
- SAPS-WS structured the trough poleward region
- SAPS-WS developed as a response to auroral processes

Correspondence to:
I. Horvath,
ihorvath@itee.uq.edu.au

Citation:
Horvath, I., and B. C. Lovell (2016), Structured subauroral polarization streams and related auroral undulations occurring on the storm day of 21 January 2005, *J. Geophys. Res. Space Physics*, *121*, 1680–1695, doi:10.1002/2015JA022057.

Received 20 OCT 2015
Accepted 29 JAN 2016
Accepted article online 3 FEB 2016
Published online 19 FEB 2016

Structured subauroral polarization streams and related auroral undulations occurring on the storm day of 21 January 2005

Ildiko Horvath[1] **and Brian C. Lovell**[1]

[1]Security and Surveillance Research Group, School of Information Technology and Electrical Engineering, University of Queensland, Brisbane, Queensland, Australia

Abstract We investigate structured subauroral polarization streams (SAPS) and their impacts on the midlatitude trough and auroral regions during the 21–22 January 2005 geomagnetic storm. This was a storm with two sudden commencements occurring under varying interplanetary magnetic field (IMF) conditions and three main phases, two of them unfolding during northward IMF. Its onset at ~1700 UT allowed us to investigate SAPS wave structures (WS) and their impacts during the local evening hours under both southward and northward IMF conditions in the American sector. Results suggest that during southward IMF, SAPS-WS might be related with standing (toroidal) Alfven waves and structured most intensively the stagnation trough. During northward IMF, the trough was created by SAPS electric (**E**) field effects only and became less structured by SAPS-WS that were of Alfvenic origin. Auroral wave structures and undulations occurred in the structured and unstructured oval regions, respectively, and triggered the subauroral region's response to produce SAPS-WS. Spectrogram images (only one shown) confirmed ring current injections implying magnetotail reconnections during the four SAPS-WS events investigated. Periodic tail connections are also evidenced by the periodic increases seen in both the solar wind-magnetosphere coupling function (ε) and the energy input efficiency. Finally, we conclude for the time period investigated that (1) the nature of SAPS-WS was informative of IMF orientation, (2) plasma stagnation enhanced SAPS **E** field and SAPS-WS development, and (3) more efficient energy input into the magnetosphere contributed to the better development of auroral undulations and SAPS-WS.

1. Introduction

The storm time subauroral ionosphere is a dynamic region. In the evening sector, a fraction of region 2 (R2) field-aligned currents (FACs) flow into the ionosphere near the auroral oval's equatorward boundary and R1 FACs flow out at the poleward boundary [*Anderson et al.*, 2001]. Pedersen currents maintain current continuity and generate large northward (or poleward) polarization electric (**E**) fields. Via their interaction with the geomagnetic **B** field (i.e., $\mathbf{E}\times\mathbf{B}$), these polarization **E** fields provide the underlying driving mechanism by driving plasma flows rapidly in the westward (or sunward) direction and thus forming ion drifts and polarization streams [*Foster and Burke*, 2002]. These large sunward (or westward) plasma flows are distinctly separated from the sunward (or westward) auroral convection of the standard Volland-Stern two-cell pattern [*Stern*, 1975; *Volland*, 1978]. Furthermore, these subauroral sunward flows reach supersonic speeds (1 to 5 km/s) and are specified differently in the literature such as polarization jets [*Galperin et al.*, 1974] and subauroral ion drifts [*Spiro et al.*, 1979], both appearing in the premidnight magnetic local time (MLT) sector (2000–2400 MLT). Recently, the terminology of subauroral polarization stream (SAPS) [*Foster and Burke*, 2002] was introduced in order to include the broader (up to 5°) sunward maximum flows developing on the duskside (1600–2000 MLT).

Focusing on the duskside, SAPS are associated with magnetosphere-ionosphere coupling and develop where R2 FACs close poleward across the low-conductance gap [*Anderson et al.*, 1993; *Foster and Burke*, 2002], where the midlatitude trough develops [*Muldrew*, 1965; *Moffett and Quegan*, 1983; *Rodger et al.*, 1992]. SAPS-related sunward (or westward) drifts tend to maximize in the low conductivity region of the trough, which is a narrow region (few latitude degrees) of reduced plasma density extending azimuthally [*Moffett and Quegan*, 1983; *Rodger et al.*, 1992; *Lee et al.*, 2011]. Trough development in the subauroral region can be due to different processes. During the local premidnight hours, westward flows in the auroral oval are opposed by eastward plasma flows in the corotating region and thus give rise to plasma flow stagnations. These lead to O^+ loss by dissociative recombination with N_2 and O_2, and to plasma depletion producing a deep trough [*Knudsen*, 1974; *Spiro et al.*, 1979]. However, in the presence of large **E** field, **E** × **B** plasma motion can advect ionospheric plasma with very different characteristics [*Foster*, 1993; *Foster et al.*, 1994], while chemical recombination of ions can reduce plasma densities and also produce a deep trough [*Schunk et al.*, 1976].

SAPS-related sunward plasma drifts are also characterized by enhanced ion and electron temperatures, both decreasing plasma densities. Enhanced ion temperatures are due to collisions between drift particles and neutral atoms, and frictional heating enhances recombination rates [*Schunk et al.*, 1976]. Enhanced electron temperatures are due to plasmaspheric heating [*LaBelle and Treumann*, 1988] that can be explained with lower hybrid (LH) wave-particle interaction [*Mishin and Burke*, 2005]. This heating occurs specifically in the equatorial plane. Part of it is carried along the magnetic field lines down to the topside ionosphere by high thermal conductivity and LH wave activity [*Mishin and Burke*, 2005]. Standard Coulomb collisions, suggested by previous studies [e.g., *Kozyra et al.*, 1987], cannot rise electron temperatures sufficiently within the required time period (~1 h) [*Mishin and Burke*, 2005]. Consequential vibrational mechanism enhances also recombination rates and deepens the trough. Unfolding as an ionospheric feedback mechanism, accelerated by low plasma densities, ionospheric conductivity becomes reduced leading to increases in enhanced SAPS **E** field and to a deeper trough [*Foster and Vo*, 2002].

Occasionally, both the SAPS feature and the plasmapause are associated with the poleward trough wall [*Huang et al.*, 2001]. Under such conditions, the trough appears narrow in latitudes and with a well-defined and well-developed poleward edge [*Muldrew*, 1965; *Moffett and Quegan*, 1983; *Rodger et al.*, 1992; *Lee et al.*, 2011]. When the SAPS **E** field erodes the cold plasmasphere and produces an erosion plume in the magnetosphere [*Foster et al.*, 2002], storm-enhanced densities (SED) [*Foster*, 1993] are created in the ionosphere, appearing on the equatorward edge of the trough. In the ionosphere, the erosion plume appears as SED plume [*Su et al.*, 2001]. By flowing across the dayside cusp region and into the polar cap, the SED plume supplies the necessary plasma for the formation of a polar tongue of ionization (TOI) [*Foster et al.*, 2005] or polar cap patches [e.g., *Zhang et al.*, 2013].

Recent studies, based on satellite and radar observations, show that both the SAPS and the trough can be quite irregular, displaying structures [*Erickson et al.*, 2002; *Mishin et al.*, 2002, 2003, 2004; *Foster et al.*, 2004]. Their resultant features are specified as SAPS wave structures (SAPS-WS) [*Mishin et al.*, 2003; *Mishin and Burke*, 2005] and irregular troughs [*Mishin et al.*, 2004; *Mishin and Burke*, 2005]. An irregular trough can be characterized by an equatorward part marked by enhanced electron temperatures and by a poleward part coinciding with strong SAPS-WS, ring current precipitations, and strong vertical ion flows [*Mishin et al.*, 2004].

SAPS-WS' underlying physical mechanisms can be kinetic Alfven waves amplified by ionospheric feedback mechanisms [*Streltsov and Mishin*, 2003; *Streltsov and Foster*, 2004] or the combination of Alfven, electromagnetic ion-cyclotron (EMIC) and electrostatic waves [*Mishin et al.*, 2003]. The growth of EMIC waves becomes enhanced after fresh ion injections from the magnetotail and becomes maximized within the regions of cold plasmaspheric plumes and along the plasmapause [*Jordanova et al.*, 2007]. Strong SAPS-WS (i.e., $|\delta V_W| \geq |\langle V_W \rangle|$, where V_W is the SAPS-related westward or sunward drift [*Mishin et al.*, 2003, 2004]) are particularly interesting. Their appearances usually follow the events of fresh ion injections, when ions from energetic plasma particles are injected from the magnetotail into the inner magnetosphere. Such events imply also magnetotail reconnection as the ions injected travel across the tail as plasma jets [*Mishin*, 2013]. These newly injected particles increase the ring current [*Huang et al.*, 2004], and thus, SAPS-WS are also regarded as standard signatures of particle injections [*Mishin et al.*, 2004].

In this study we focus on SAPS-WS occurring in the North American sector during the 21 January 2005 geomagnetic storm. Our main aim is to investigate how the development of midlatitude trough and auroral zone became impacted by the simultaneously occurring SAPS-WS. Results show that (1) SAPS-WS significantly enhanced and structured the trough's poleward edge, (2) SAPS-WS impacted more intensively the stagnation trough than the trough created by chemical recombination only, (3) SAPS-related sunward drift was stronger in the deeper stagnation trough due to the feedback mechanisms, and finally (4) SAPS-WS developed as a response to auroral processes.

2. Database and Methodology

Our multi-instrument database contains ground- and space-based data and some model simulations. For tracking ionospheric features, we have utilized Global Positioning System (GPS) total electron content (TEC; total electron content unit (TECU) where 1 TECU = 10^{16} el/m^2) values from the global network of 402 ground-based GPS stations operating at that time. These GPS TEC values are from Haystack Observatory's Madrigal Database.

We have also utilized multi-instrument in situ measurements from Defense Meteorological Satellite Program's (DMSP) spacecraft F13 on 0545–1745 LT orbit and F14–F15 on 0928–2128 LT orbits at ~840 km altitude. DMSP measurements include ion density (Ni; i^+/cm^3), electron and ion temperature (Te and Ti, K), cross-track plasma drifts (V_Y, V_Z; m/s) in the east-west horizontal or zonal (Y) and north-south or vertical (Z) directions, and their respective cross-track plasma flows (F_Y, F_Z; i^+/(cm^2 s)) computed as Ni × V. We have also made use of DMSP spectrograms and automated boundary identifications provided by The John Hopkins University/Applied Physics Laboratory (JHU/APL) in order to identify plasma regimes. Based on the work of *Newell et al.* [1996], central plasma sheet (CPS) and boundary plasma sheet (BPS) region identifications were utilized for the dayside. For the nightside, direct boundary identifications were carried out by utilizing various equatorial (b1e, b2i, and b2e) and poleward (b5) boundary parameters. Regardless of local time, the plasmapause (marked as PP) coincides with b1e, and the b4s parameter marks the boundary of structured and unstructured auroral regimes. For specifying auroral oval boundary positions, we have used data provided by the Oval Variation, Assessment, Tracking, Intensity, and Online Nowcasting (OVATION) project.

For monitoring the underlying geomagnetic activity, we have employed a small collection of geomagnetic indices. These include the 1 min time resolution *SYM-H*, *ASY-H*, and *AE* data (in nT) plus the 3 h *Kp* values. This study's ionospheric observations are obtained for the magnetically disturbed day of 21 January 2005 ($\Sigma Kp = 35-$).

Obtained from the Coordinated Community Modelling Centre (CCMC) by requesting online runs, we have also employed a small collection of model simulations. These are from the Coupled Thermosphere-Ionosphere-Plasmasphere electrodynamics (CTIPe) model [*Fuller-Rowell et al.*, 2002] and from the Thermosphere Ionosphere Electrodynamic General Circulation Model (TIE-GCM) [*Richmond et al.*, 1992]. Model outputs include the CTIPe-generated solar power (P_{solar}; W/kg) data and the TIE-GCM-generated Joule heating (Q_{Joule}; W/kg) data.

We have also made use of interplanetary magnetic field (IMF) and solar plasma measurements taken by the Advanced Composition Explorer (ACE) satellite that was positioned at ~(222.51; −35.47; 21.69) R_E in GSE coordinate system. A ~25 min extra time was added to the ACE data to allow comparison between IMF and geomagnetic signatures. The solar wind motional zonal **E** field (IEF $\mathbf{E_Y}$; mV/m) was computed as $-\mathbf{V_X} \times \mathbf{B_Z}$ [*Mannucci et al.*, 2005], where $\mathbf{V_X}$ (km/s) is the solar wind velocity in the X direction and $\mathbf{B_Z}$ (nT) is the IMF's vertical or Z component. By employing the 15 min polar cap north (PCN; mV/m) index from Thule (290.83°E, 77.48°N; geographic), we have also modeled the cross polar cap potential (PCP) drop as Φ_{PC} (kV) = 19.35PCN + 8.78 [*Troshichev et al.*, 1996]. Solar wind kinetic energy (U_{SW}; GW where $G = 10^9$), the ultimate energy source, was computed as U_{SW} $(GW) = ½\rho(V_{\text{SW}})^3 A$ [*Shue et al.*, 1997]. Here ρ and V_{SW} are the mass density and the bulk velocity of the solar wind, respectively, and A is the cross section of the dayside magnetosphere by assuming a cylindrical symmetric configuration and taking the magnetotail radius as $X_{\text{GSM}} = -30\,R_E$ [*Petrinec and Russell*, 1996]. For determining the solar wind energy coupling rate, we have computed the energy coupling function, also known as the epsilon (ε) parameter, as $\varepsilon\ (GW) = (4\pi/\mu_o)\, V_{\text{SW}} B^2 (l_o)^2 \sin^4(\theta/2)$, where μ_o is the magnetic permeability, V_{SW} is the solar wind speed, B is the IMF magnitude computed as $(B_Y{}^2 + B_Z{}^2)^{1/2}$, l_o is 7 R_E, and θ is the clock angle derived from $\tan(\theta) = B_Y/B_Z$ [*Perreault and Akasofu*, 1978; *Akasofu*, 1981]. Finally, energy input efficiency (EI$_{\text{eff}}$; %) was computed as $(\varepsilon/U_{\text{SW}}) \times 100\%$ [*Li et al.*, 2012; *Wang et al.*, 2014].

3. Observations and Interpretations

3.1. 21–22 January 2005 Geomagnetic Storm Events

Figure 1 is constructed with a variety of ACE and geomagnetic data and illustrates the nature of the 21–22 January 2005 solar and geomagnetic events. This storm is characterized by two sudden storm commencements (indicated as SSC-1 and SSC-2) and three main phases (indicated as main phase-1, main phase-2, and main phase-3). A large coronal mass ejection (CME) arrived at the magnetopause at ~1712 UT on 21 January triggering SSC-1. Its signature is the sudden increase of geophysical indices such as *ASY-H*, *SYM-H*, and *AE* while $\mathbf{B_Z}$ turned northward. SSC-2 occurred at 1900 UT when *ASY-H* increased from −41 to 45 nT.

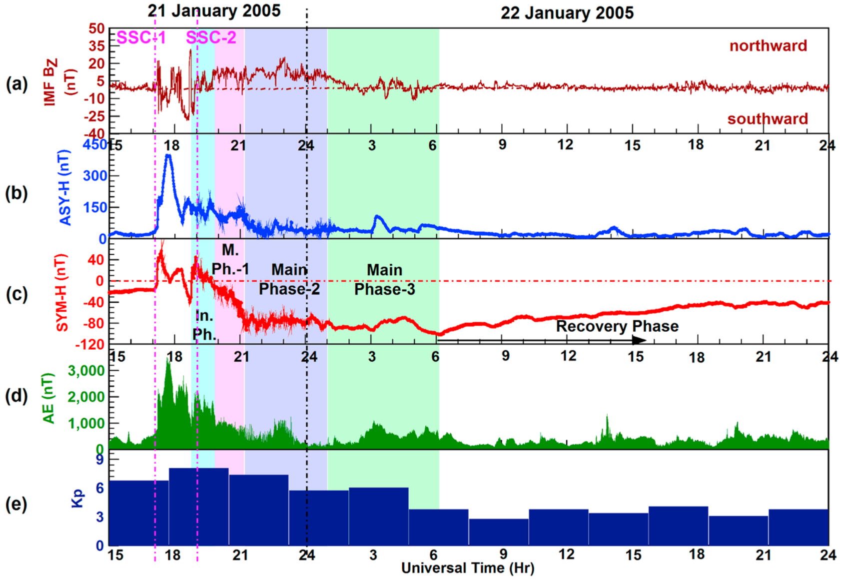

Figure 1. A small collection of line plots depicts interplanetary and geomagnetic conditions and the nature of the 21–22 January 2005 geomagnetic storm.

Then, southward $\mathbf{B_Z}$ led to the storm initial phase and subsequent main phase-1 (1946–2126 UT). During main phase-1, *SYM-H* decreased to −92 nT at 2126 UT and remained at around −80 nT during the following main phase-2 (2126–0124 UT) that, in turn, was followed by main phase-3 beginning at ~0124 UT on the next day of 22 January [*Du et al.*, 2008]. During main phase-3, *SYM-H* reached its minimum of −101 nT at ~0608 UT on 22 January. What makes this geomagnetic storm even more unusual is that at the onset of main phase-1 (~1946 UT), $\mathbf{B_Z}$ turned northward and remained northward directed during main phase-1 and main phase-2. Another interesting feature is the prolonged minimum occurring in the ring current that can be seen in the *SYM-H* profile as a flat phase (around −80 nT) [*Du et al.*, 2012]. This feature was created by the magnetosphere's extreme compression due to solar wind flux [*Kalegaev et al.*, 2015].

3.2. SAPS-WS Event During the Initial Phase

Figure 2 depicts the response of the northern ionosphere to the initial phase and a SAPS-WS event occurring at around 1845 MLT under southward $\mathbf{B_Z}$ conditions. In Figure 2a, the line plots of TIE-GCM-generated Q_{Joule} and CTIPe-generated P_{solar} illustrate the longitudinal variations of Joule heating and solar heating, respectively, along 80°N (geographic). This is the latitude of the magnetic North Pole, of which location is marked in the Northern Hemisphere map (see Figure 2b). In this map, the modeled magnetic meridians, magnetic and dip equators, and the ground track of an ascending F14 pass that followed one of the magnetic meridians over the North Atlantic are also plotted. Auroral oval boundaries are plotted by utilizing OVATION data. These figures illustrate that both Q_{Joule} and P_{solar} peaked (500 W/kg and 2.5 W/kg, respectively) close to the magnetic pole. Meanwhile, P_{solar} remained high in a larger region around the magnetic pole implying that the polar cap was sunlit at 1615 LT. Maximizing Q_{Joule} implies that due to dayside reconnection, the magnetic pole received from the magnetosphere some large amounts of electromagnetic energy that had been dissipated as Joule heating [*Huang et al.*, 2014]. Meanwhile, the GPS TEC map depicts the topology of the northern ionosphere during this time. As labeled, the ionospheric features tracked include a large SED bulge (22–26 TECU; indicated in light green) over North America and a well-developed SED plume (8–13 TECU; indicated in yellow) forming a polar TOI [*Foster et al.*, 2002, 2004] and also providing plasma for some polar patches [*Zhang et al.*, 2013].

In Figure 2c, a set of line plots is constructed with the in situ data recorded by F14. First, the Ni plot depicts a latitudinal profile of the topside ionosphere over the North Atlantic. The ionospheric features tracked include a small SED feature ($25 \times 10^3\ i^+/\mathrm{cm}^3$), the midlatitude trough ($2 \times 10^3\ i^+/\mathrm{cm}^3$), some auroral ionization, and the polar TOI reaching $85 \times 10^3\ i^+/\mathrm{cm}^3$ (indicated as polar cap enhancement) over the magnetic pole and showing segmentation by a large plasma depletion ($15 \times 10^3\ i^+/\mathrm{cm}^3$). These Ni data are also plotted over the GPS TEC map (see Figure 2b).

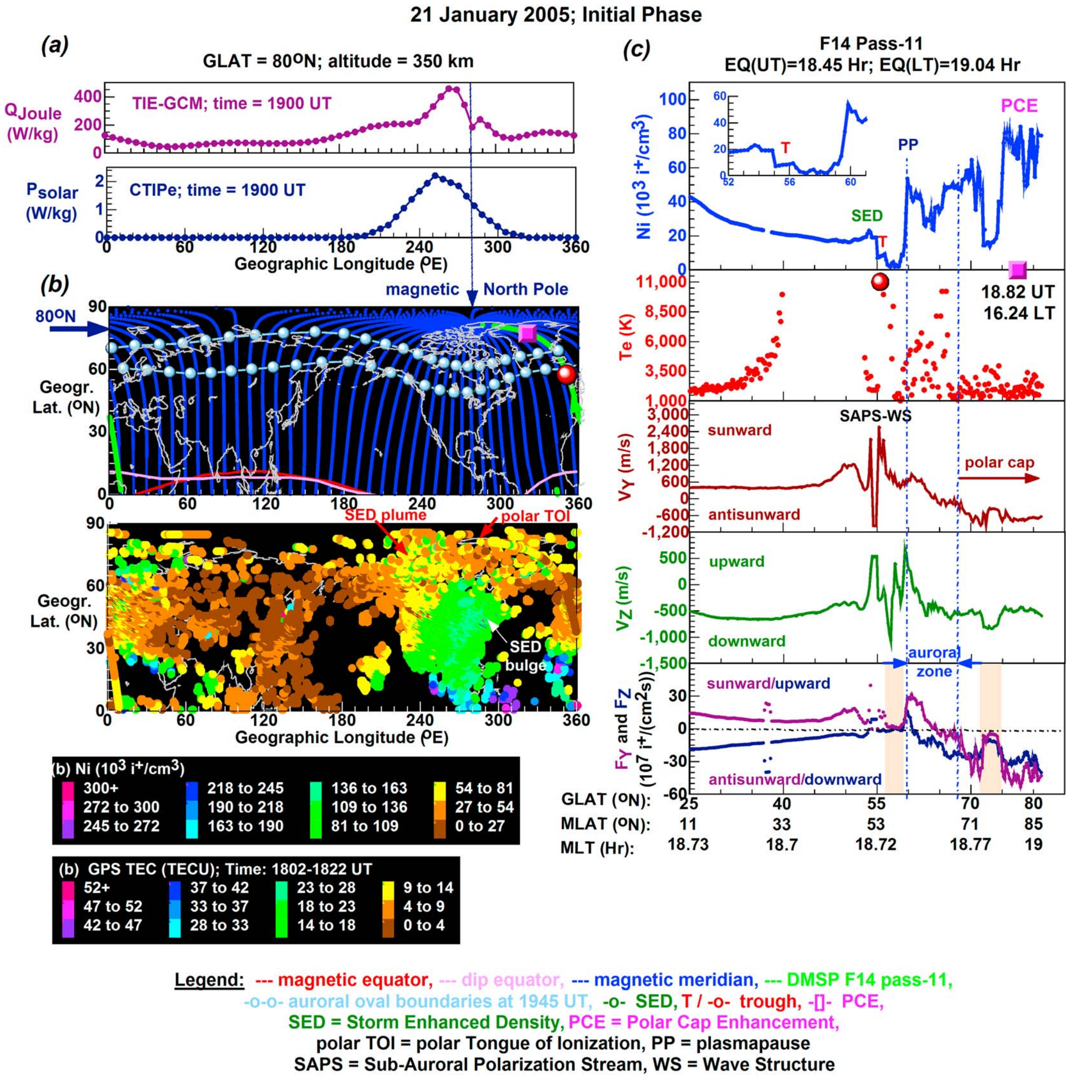

Figure 2. The various aspects of ionospheric response to the storm initial phase in the American sector on 21 January 2005 is illustrated with (a) the TIE-GCM Q_{Joule} and CTIPe P_{solar} line plots generated for magnetic north pole latitude, (b) the northern maps illustrating the auroral oval boundaries, magnetic and dip equators, ground track of F14 providing topside measurements, and the spatial distribution GPS TEC, (c) the multi-instrument F14 line plot sets tracking a stagnation trough and polar TOI plus a SAPS-WS, manifesting the combination of standing (toroidal) Alfven waves and EMIC waves, and their various thermal, drift, and plasma flow signatures. The shaded intervals indicate flow stagnation.

Although there are data gaps, the Te line plot depicts the subauroral Te peak (11,000 K) that defines the coinciding locations of trough minimum and plasmapause [*Prolss*, 2006]. Plasmapause location was also confirmed by the b1e boundary. Some significantly lower Te values (2500 K) in the polar cap region indicate that the cold SED plume plasma became transported by antisunward plasma flows across the polar cap region where it formed a polar TOI [*Foster et al.*, 2002, 2004].

Meanwhile, the V_Y and V_Z line plots tracked in the SAPS channel a well-developed and strong SAPS-WS (1845 MLT; 1845 UT; 1800 LT) that could be due to the combination of Alfven and EMIC waves. The reason is that a strong SAPS-WS like this is most likely a spatial (not a temporal) structure. Mainly, it could be due to standing (toroidal) Alfven waves [*Mishin and Burke*, 2005]. However, we speculate that EMIC waves also contributed to its development [*Mishin et al.*, 2003]. EMIC waves frequently occur in plasmaspheric plumes wherein the irregular internal structures provide growth regions [*Morley et al.*, 2009]. As EMIC waves map down along the magnetic field lines to the topside ionosphere, the plasmapause can also be a preferred location of EMIC waves [*Fraser and Nguyen*, 2001; *Yuan et al.*, 2012]. As this scenario illustrates, the sunward V_Y maximized

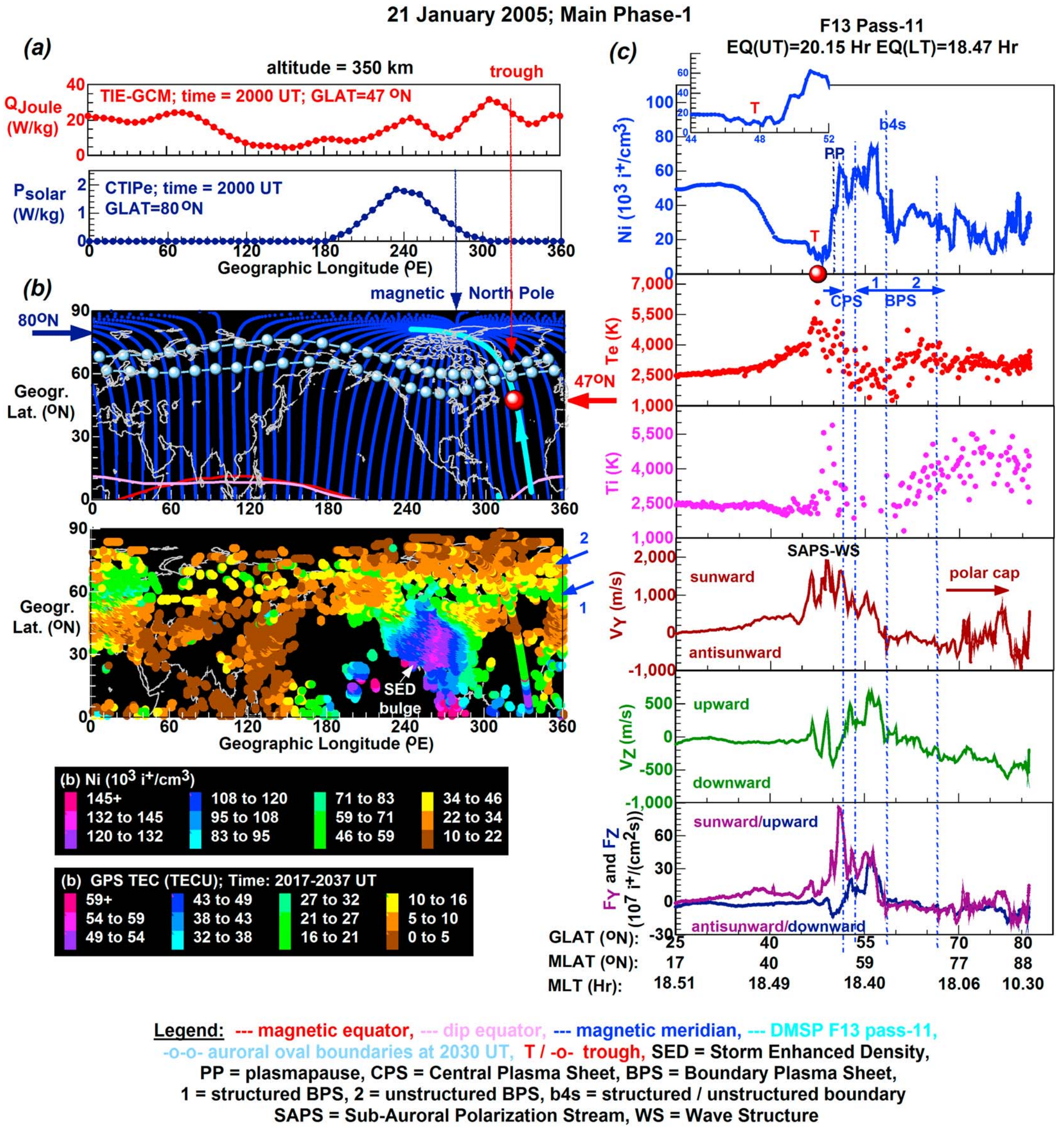

Figure 3. Same as Figure 2 but for a main phase-1 scenario with TIE-GCM Q_{Joule} data generated for trough latitude and for a SAPS-WS of Alfvenic origin.

at 2800 m/s and the upward V_Z reached 600 m/s at trough latitudes and in the structured SAPS channel but the upward drift maximized (700 m/s) in the auroral zone. The impact of SAPS-WS on the trough (see enlarged Ni plot section) appears as fluctuations of relatively higher and lower plasma densities marking the corresponding relatively higher and lower height integrated Pedersen conductivity [*Mishin et al.*, 2003].

Finally, the F_Y and F_Z line plots tracked flow stagnations (indicated as shaded areas) in two separate regions: (1) in the trough region where the eastward corotation canceled out the westward convection of the two-cell polar convection [*Knudsen*, 1974; *Spiro et al.*, 1979] and also (2) in the polar cap region where flow stagnation segmented the polar TOI [*Brinton et al.*, 1978; *Sojka et al.*, 1991]. These observations provide evidence that the trough was a stagnation trough and R2 FAC-related strong frictional heating further enhanced recombination rates and thus further deepened the trough while the SAPS **E** field became stronger [*Foster and Vo*, 2002] and structured [*Mishin et al.*, 2003]. During this self-accelerating process, the SAPS-WS developed with a maximum V_Y of 2600 m/s.

3.3. SAPS-WS Events and Moderate Auroral Undulations During Main Phase-1

Figure 3 is constructed the same way as Figure 2 for direct comparisons and depicts a SAPS-WS event occurring under northward $\mathbf{B_Z}$ conditions during the first main phase at 1820 MLT. As this scenario occurred under northward $\mathbf{B_Z}$ conditions, when dayside reconnection stopped or became minimal (see details in section 4.1), the Q_{Joule} line plot was constructed for 47°N (geographic) where the trough developed.

In Figure 3a, the Q_{Joule} line plot tracked close to maximum values (25 W/kg) over the North Atlantic, where the trough became embedded in a SAPS-WS, and thus indicates energy inputs from the magnetosphere. Furthermore, the P_{Solar} line plot constructed for polar latitude indicates that the magnetic pole received little solar radiation as the peak occurred away from the magnetic pole. In Figure 3b, the GPS TEC map tracked the SED bulge (43–49 to 54–59 TECU; indicated in dark blue to pink, respectively) that appeared to be better developed during this main phase scenario than before (see Figure 2b). But there was no SED plume entering the polar cap region through the dayside cusp, and thus, the polar TOI was absent. During this scenario, the northward $\mathbf{B_Z}$ and the rapidly slowing polar convection (see details in section 4.2) prevented polar TOI development, which usually requires southward $\mathbf{B_Z}$ orientation and strong convective plasma flows [*Foster et al.*, 2005]. Meanwhile, the TEC map depicts very clearly a double band appearing in the auroral oval due to the structured and unstructured (marked as 1 and 2, respectively) regions of the BPS. These regions have higher TEC (27–32 TECU; indicated in light green) and lower TEC (10–16 TECU; indicated in yellow) respectively. This interpretation is verified with the line plot sets of Figure 3c.

In Figure 3c, the Ni line plot tracked the plasma density features appearing over the North Atlantic. We have marked the lower latitude CPS and higher latitude BPS, which correspond largely to the diffuse and discrete aurorae, respectively [*Winningham et al.*, 1975], and the polar cap. A magnified Ni section of the trough bottom ($10 \times 10^3\ i^+/\mathrm{cm}^3$) shows some SAPS-WS-related plasma density fluctuations. Maximized electron (6500 K) and ion (5500 K) temperatures mark the trough minimum. These provide observational evidence and thus support the above described Q_{Joule} detection suggesting that there was some strong energy input into the ionosphere at trough latitudes dissipating as Joule heating and therefore increasing ion temperatures. Furthermore, some significant heat had been generated in the ring current/plasmasphere overlap region elevating electron temperatures [*Mishin and Burke*, 2005]. Meanwhile, the V_Y and V_Z line plots tracked a large SAPS-WS (1820 MLT; 2030 UT; 1730 LT). In the structured SAPS channel, the sunward drift reached 2000 m/s and V_Z varied between 550 and −450 m/s. Since the V_Y variations have similar frequencies, they could be due to Alfvenic perturbations [*Mishin et al.*, 2003]. This suggests, in accordance with the basic SAPS mechanisms [*Foster and Burke*, 2002; *Foster and Vo*, 2002], that as the downward R2 FAC shifted equatorward, the SAPS **E** field increased and became structured [*Mishin and Mishin*, 2007]. An interesting feature is the structured sunward drifts in the CPS and BPS implying that auroral processes triggered SAPS-WS development as a subauroral response. This is further suggested by the strong similarity between the SAPS-WS and the structured sunward convection in the CPS and BPS. This similarity implies also that these auroral and subauroral features are interrelated. Regarding the F_Z and F_Y line plots, the lack of flow stagnations at trough latitudes indicates that this trough formed mainly due to the strong SAPS **E** field-related plasma drifts and frictional heating that in turn enhanced ionospheric recombination rates [*Foster and Vo*, 2002]. We note that this SAPS-WS observation will be further analyzed (see section 4.1).

Figure 4 illustrates in the same format another main phase-1 SAPS-WS event occurring at around 2030 MLT under northward $\mathbf{B_Z}$ conditions. Because of the similar UT but different LT recordings, this figure depicts how the previous SAPS-WS shown in Figure 3 had changed as the magnetic local time progressed from 1820 to 2030 MLT. During this scenario, Q_{Joule} at trough latitude (50°N) was lower (15 W/kg) than before over the North Atlantic. Furthermore, the P_{Solar} values were close to minimum over the magnetic pole indicating that the polar cap received almost no solar radiation (see Figure 4a). This is also evident from the GPS TEC map tracking minimum TEC (0–6 TECU; indicated in dark brown) at around the magnetic pole. Meanwhile, the double band in the auroral zone is still noticeable and is due to the structured and unstructured (marked as 1 and 2, respectively) auroral regions. Their respective regions of higher TEC (30–36 TECU; indicated in light green) and lower TEC (12–18 TECU; indicated in yellow) are more obvious over Europe and Asia. Although the SED bulge (48–54 to 60–66 TECU, indicated in dark blue to pink, respectively) became better developed than before (see Figure 3b), there was no SED plume because of the unfavorable polar convection conditions created by northward $\mathbf{B_Z}$ (see details above).

In Figure 4c, the Ni line plot tracked the ionospheric features appearing over the North Atlantic. These include a narrow trough region ($10 \times 10^3\ i^+/\mathrm{cm}^3$) appearing with a steep poleward wall, which is the signature of plasmapause (see details below), and a low plasma density ($15 \times 10^3\ i^+/\mathrm{cm}^3$) region equatorward of the trough. Both of these regions were quite structured as the magnified Ni section reveals. Furthermore, plasma

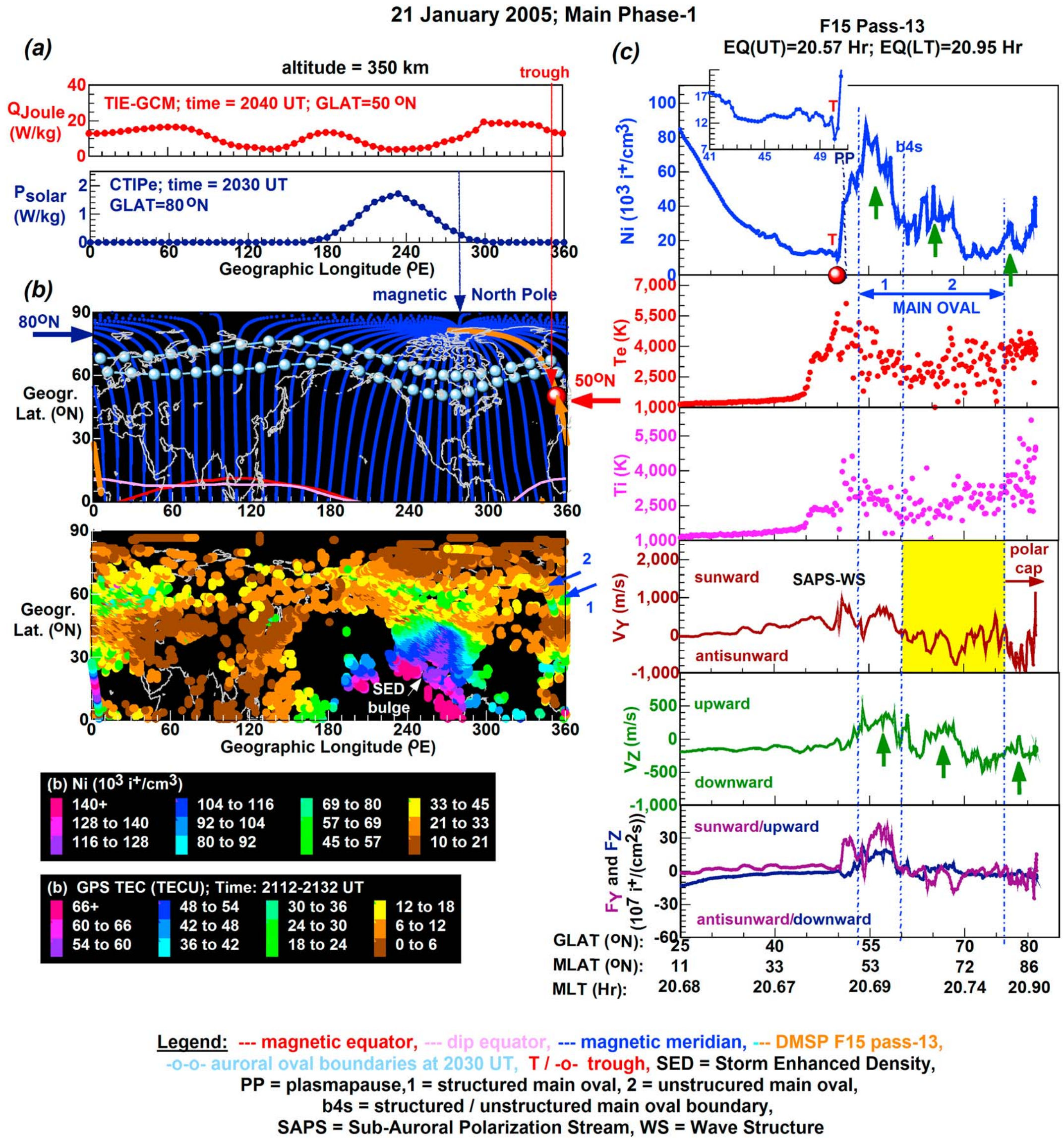

Figure 4. Same as Figure 3 but for another main phase-1 scenario during which the SAPS-WS of Alfvenic origin was triggered by moderate auroral undulations (indicated as shaded interval in yellow) in the unstructured auroral region. Arrows indicate upward drifts increasing plasma densities.

densities were twice as large in the structured oval region (marked as 1; Ni $\approx 90 \times 10^3$ i^+/cm^3) than in the unstructured oval region (marked as 2; Ni $\approx 45 \times 10^3$ i^+/cm^3). Additionally to the b1e boundary coinciding with the plasmapause, both the subauroral Te peak (6000 K) and the steep poleward trough wall indicate also that the plasmapause was located at the poleward trough wall. According to the subauroral Ti peak (4500 K), there was still energy input into the subauroral ionosphere at trough latitudes that dissipated as Joule heating. Furthermore, the SAPS-WS was less developed than before (see Figure 3c) and sunward drifts peaked at 1000 m/s only. But the impact of SAPS-WS on the trough bottom is still visible (see enlarged Ni section). Moreover, the V_Y line plot tracked in the unstructured oval region (marked as 2) some auroral undulations or ion waves (see shaded interval in yellow) that are due to auroral surges or streamers [*Henderson et al.*, 2010]. These simultaneous observations of SAPS-WS and auroral undulations provide further demonstrations that auroral undulations cause SAPS-WS. Meanwhile, the V_Z line plot tracked some large-scale periodic upward drifts in the auroral and polar regions contributing to the development of large plasma density increases occurring there by moving the ionization to higher altitude where recombination rates are low. Finally, the F_Z and F_Y line plots provide evidence that the trough was not a stagnation trough.

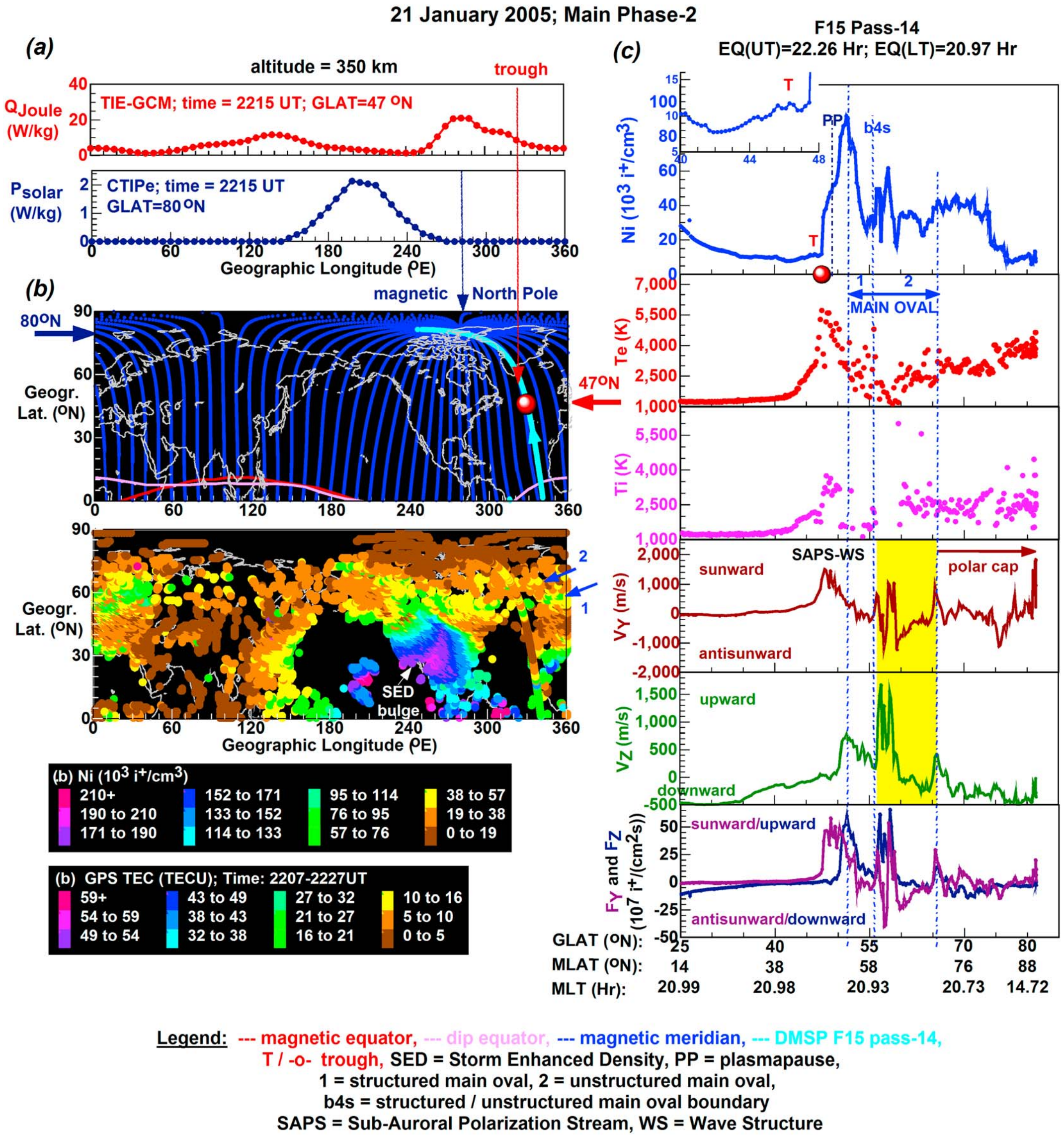

Figure 5. Same as Figure 4 but for a main phase-2 scenario during which the SAPS-WS of Alfvenic origin was triggered by intensive auroral undulations (indicated as shaded interval in yellow) in the unstructured auroral region.

3.4. SAPS-WS Event and Intensive Auroral Undulations During Main Phase-2

Figure 5 illustrates in the same format a main phase-2 SAPS-WS event occurring at around 2055 MLT under northward $\mathbf{B_Z}$ conditions. Due to the similar LT and MLT but different UT covered, this figure illustrates how the SAPS-WS and auroral undulations shown in Figure 4 had changed as the universal time progressed from ~2100 to ~2230 UT. During this scenario, the Q_{Joule} data indicate some small (10 W/kg) Joule heating over the North Atlantic at 47°N where the trough-SAPS-WS developed. According to the close to minimum P_{Solar} values over the magnetic pole, the polar cap received almost no solar radiation (see Figure 5a). This is also apparent in the minimum TEC (0–6 TECU; indicated in dark brown) tracked in the polar cap around the magnetic pole. Forming a double band in the auroral zone, there are some higher TECs (30–36 TECU; indicated in light green) in the structured (marked as 1) auroral region and some lower TECs (12–18 TECU; indicated in yellow) in the unstructured (marked as 2) auroral region. These regions are particularly obvious over the North Atlantic and Europe. Furthermore, the SED bulge (43–49 to 54–59 TECU, indicated in dark blue to pink, respectively) became less developed than before (see Figure 4b).

Shown in Figure 5c, the latitudinal Ni profile tracked some of the above described features over the North Atlantic. Similarly to the previous scenario (see Figure 4c), a narrow trough ($10 \times 10^3\ i^+/\mathrm{cm}^3$) and a low plasma density ($7 \times 10^3\ i^+/\mathrm{cm}^3$) equatorward region developed. As the magnified Ni section reveals, the plasma density was quite structured there. Meanwhile, a large plasma density enhancement comprised the trough's poleward side reaching $90 \times 10^3\ i^+/\mathrm{cm}^3$. These high plasma densities were rapidly decreasing (from 90×10^3 to $30 \times 10^3\ i^+/\mathrm{cm}^3$) in the structured oval region (marked as 1). Again, the subauroral Te peak (5800 K) marks the trough minimum, and the steep poleward trough wall and b1e indicate the plasmapause. Compared to the previous scenario (see Figure 4c), a smaller subauroral Ti peak (3800 K) indicates here some smaller energy input into the subauroral ionosphere at trough latitudes dissipating as Joule heating. However, this energy input resulted in a better developed SAPS-WS that was possibly generated by Alfven waves. Within the SAPS-WS, the sunward drifts peaked at 1600 m/s impacting the trough bottom and its equatorward region as well. However, there was no V_Z oscillation in the structured SAPS channel, and flow stagnation was also absent according to the F_Z and F_Y line plots. But in the unstructured oval region (marked as 2) both the V_Y and the V_Z line plots tracked significantly more rigorous ion waves or auroral undulations (indicated as shaded interval in yellow) than before (see Figure 4c). These vigorous drift structures are also known as intensive or giant auroral undulations caused by auroral surges or streamers [*Henderson et al.*, 2010]. During this scenario, these intensive auroral undulations occurred with a better developed SAPS-WS ($V_Y \approx 1600$ m/s) than before, when auroral undulations were moderate (see Figure 4c). Thus, Figure 5c provides further evidence that auroral undulations cause SAPS-WS. Similarly, intense V_Y and V_Z drift structures are reported in the recent work of *Sandholt et al.* [2014] noticing also that such drift configurations are typically associated with auroral surges or streamers.

4. Analysis

4.1. Analyzing a Main Phase-1 SAPS-WS Event

Figure 6 provides a more detailed illustration of the previously shown (see Figure 3) well-developed SAPS-WS (1828 MLT) of main phase-1. The highlighted track segment mapped indicates the region covered in the spectrogram image (see Figures 6a and 6b). The spectrogram image of downward flowing precipitating electrons and ions depicts precipitating ring current ions (indicated as Prec.-RC ions), the CPS and BPS in the auroral zone, and some soft particle precipitations in the polar cap region that are the signature of polar rain [*Winningham and Heikkila*, 1974].

Figure 6c illustrates the line plots of Ni, Te, V_Y, and V_Z that are described in section 3.3. Here we focus on some fundamental SAPS-WS features and show that the SAPS-WS appeared with fluxes of electrons and ions wherein the enhanced fluxes of precipitating ions are the signature of precipitating ring current ions [*Mishin et al.*, 2004]. Thus, a well-developed SAPS-WS is a good indicator of ring current injections [*Mishin and Burke*, 2005]. This scenario shows also that the entire trough became embedded in the SAPS-WS wherein the sunward drift (V_Y) reached 2000 m/s. For further analyzing the impact of SAPS-WS on the trough, we specify the equatorward and poleward trough regions (indicated as shaded intervals in light green and light blue, respectively) by considering the location of trough minimum that is marked by the subauroral Te (6500 K) peak. In the poleward trough region, which is between the trough minimum and the plasmapause (marked as PP), some irregular and increasing solar-produced plasma densities occurred with some moderate positive plasma density gradients and elevated Te (~5000 K). Furthermore, this poleward trough region is also the region of precipitating ring currents and of high sunward drift ($V_Y > 1000$ m/s) and vertical drift ($-400\ \mathrm{m/s} < V_Z < 400$ m/s). Because of this colocation and the closeness of the plasmapause, we speculate that these plasma density features of the poleward trough region could be due to the combination of gradient drift instability mechanisms underlying the SAPS-WS and shear flows at the plasmapause. Gradient drift instability mechanisms can develop when $V_Y > 500$ m/s [*Keskinen et al.*, 2004] and thus can generate positive feedback instability mechanisms inside the trough region and therefore enhance Alfven waves [*Mishin and Blaunstein*, 2008]. Shear flows at the plasmapause are driven by intense SAPS associated shear flows [*Kelley*, 1986] and structure plasma densities equatorward of the auroral zone [*Henderson et al.*, 2010]. However, both shear flows and gradient drift instability point to Kelvin-Helmholtz/interchange type instabilities [*Henderson et al.*, 2010]. Another interesting feature is the enhanced and structured sunward convections in both the CPS and the structured BPS (marked as 1) causing the development of structured SAPS. These observational

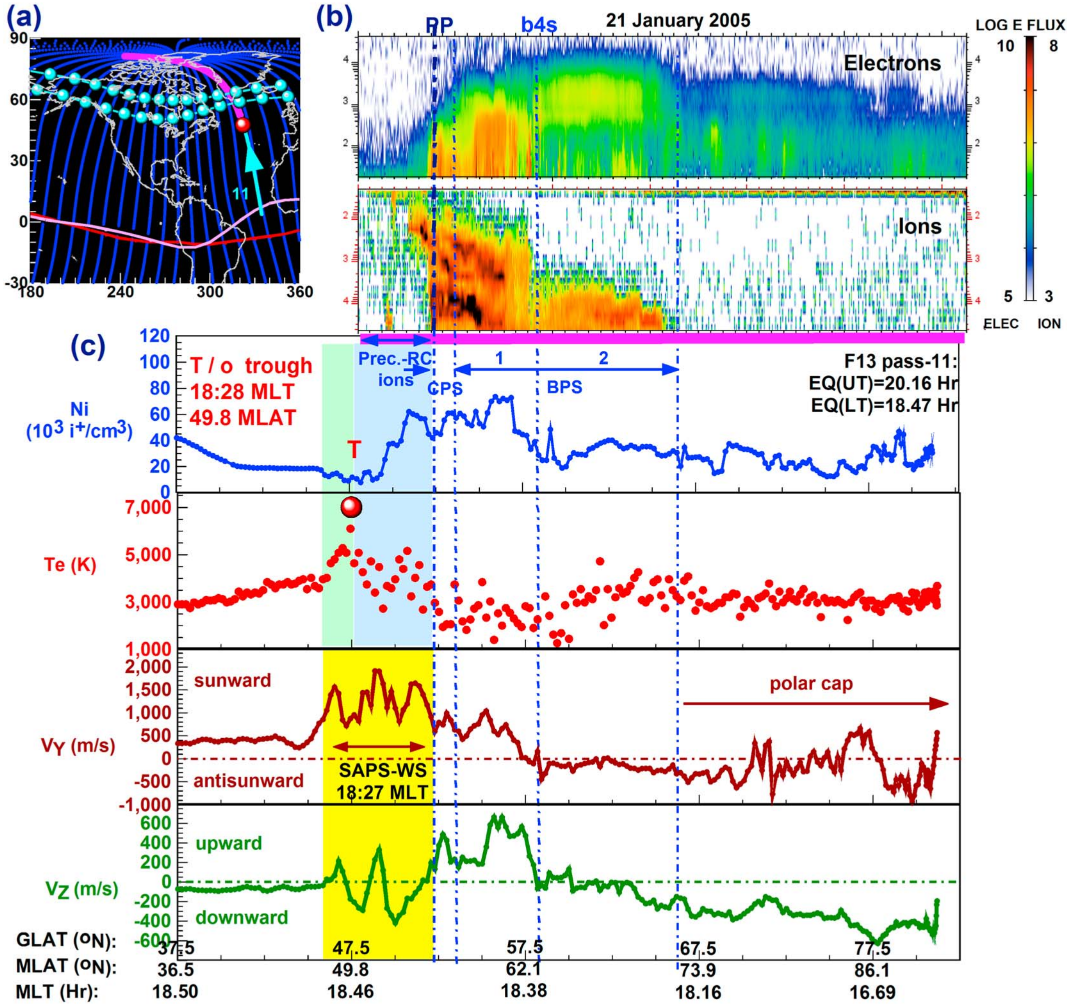

Figure 6. (a) The map shows the DMSP spacecraft's ground track passing over the magnetic North Pole while the section illustrated with spectrograms is highlighted in pink. (b) The ion and electron spectrograms tracked the signatures of precipitating ring current ions (abbreviated as Prec.-RC ions), CPS, and BPS with its structured and unstructured region-1 and region-2, respectively. (c) More detailed line plots, shown previously in Figure 3c, illustrate the structured equatorward (indicated as shaded interval in light green) and poleward (indicated as shaded interval in light blue) trough regions and the underlying SAPS-WS (indicated as shaded interval in yellow).

results are consistent with and add to previous studies [*Foster and Burke*, 2002; *Foster and Vo*, 2002] explaining the basic phenomenon of poleward directed SAPS **E** field.

4.2. Analyzing Energy Deposition Events

In Figure 7, a set of time series is constructed to illustrate the various energy deposition events taking place during the various SAPS-WS scenarios. Additionally to the IMF $\mathbf{B_Z}$ component, the parameters shown include the modeled cross PCP drop (Φ_{PC}; kV) that measures the strength of magnetosphere-ionosphere coupling and polar **E** × **B** convection [*Troshichev et al.*, 2000], and the epsilon parameter (ε; GW) that is a solar wind-magnetosphere coupling function [*Akasofu*, 1981]. Meanwhile, the energy input efficiency ($\mathrm{EI_{eff}}$; %) indicates how efficiently the solar wind energy entered the magnetosphere [*Li et al.*, 2012]. Furthermore, the time series of ΣE_Y (mV/m min) gives a measure of the accumulation of input solar wind energy, and $\Sigma SYM\text{-}H$ (nT min) is a measure of energy release [*Du et al.*, 2008]. In the line plots of ε and $\mathrm{EI_{eff}}$, we have marked (indicated as symbols "stars") when the four SAPS-WS events investigated occurred, and their UT occurrences show good correlations with the increase of both energy deposition and energy efficiency.

To describe the correlation between these ε and $\mathrm{EI_{eff}}$ peaks and SAPS-WS events, the first SAPS-WS event occurred at ~1845 UT. Then ε (6800 GW) and $\mathrm{EI_{eff}}$ (0.6%) maximized, and southward $\mathbf{B_Z}$ was strongest

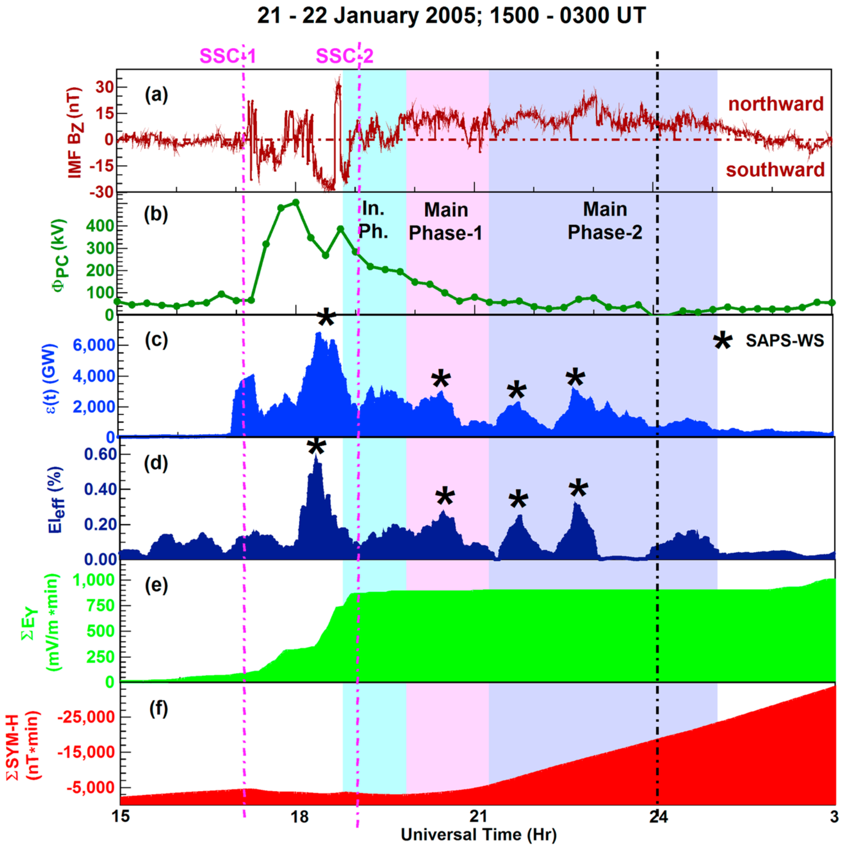

Figure 7. (a) Additionally to the IMF $\mathbf{B_Z}$ component, (b)–(f) a small collection of line plot series illustrates the temporal variations of storm time energetics. (Figure 7c) The ε parameter shows how the energy transferred from the solar wind to the magnetosphere varied, while (Figure 7c) EI_{eff} depicts the efficiency of this transfer. During a peak and three subpeak periods, the SAPS-WS events of interest (marked as symbol stars) occurred. These events provide evidence of reoccurring tail connections while (Figure 7e) dayside reconnection stopped, and thus, ΣE_Y remained constant forming a plateau from 2000 UT onward. (Figure 7f) But according to the positive gradient of Σ*SYM-H* line plot, there was continuous ring current injection.

(−30 nT). Hence, dayside reconnection allowed maximum solar wind energy deposition. However, at such a high-energy input, a substorm usually develops as the storm unfolds and energetic particles are injected from the magnetotail into the inner magnetosphere. Various substorm-associated phenomena can also occur. These include tail connection, particle injection, plasmoid formation, and auroral precipitation. These trigger the development of SAPS-WS [*Mishin and Burke*, 2005]. Regarding the next three SAPS-WS events, these coincide with some of the ε and EI_{eff} subpeaks (~3000 GW) occurring during continuous northward $\mathbf{B_Z}$. These SAPS-WS events confirm significant tail connections [*Mishin and Mishin*, 2007]. These tail connection-related energy inputs are further illustrated with the ΣE_Y line plot showing a plateau and thus indicating that solar energy input paused while $\mathbf{B_Z}$ was northward. But the positive gradient of the Σ*SYM-H* line plot indicates that there was an ongoing energy input into the ring current from 2000 UT onward.

5. Discussions

In this study we have investigated the 21 January 2005 geomagnetic storm, and four SAPS-WS events plus their causative subauroral and auroral undulations in the context of storm phases and energetics. Since each of these observations was tracked along a certain magnetic meridian over the North Atlantic, we could compare these observations and investigate their evolvement as the storm unfolded.

First, we discuss the nature of causative electromagnetic waves, which were illustrative of both the orientation of $\mathbf{B_Z}$ and the form of energy deposition. The first SAPS-WS event (see Figure 2) occurred during the initial phase under southward $\mathbf{B_Z}$ conditions, when dayside reconnection prevailed (see Figure 7).

According to the V_Y and V_Z wave patterns observed, this SAPS-WS was possibly caused by the combination of standing (toroidal) Alfven waves [*Mishin and Burke*, 2005] and EMIC waves [*Mishin et al.*, 2003], and the underlying events also support our interpretation. Regarding the standing waves, our interpretation shows a good agreement with the work of *Mishin and Burke* [2005]. Thus, we discuss here the possible presence of EMIC waves. Some compelling reasons are the strong regular two-cell polar plasma convection and the well-developed SED plume (i.e., ionospheric signature of plasmaspheric plume [*Su et al.*, 2001]) that became convected into the polar region forming a polar TOI and some polar patches as well. Under such conditions, plasmaspheric drainage plume is one of the preferred regions of EMIC wave generation [*Chen et al.*, 2009; *Yuan et al.*, 2012], and the cold plasma of drainage plume can guide EMIC waves along the magnetic field lines to the topside ionosphere [*Morley et al.*, 2009]. The next three SAPS-WS events (see Figures 3–5) occurred during the main phase and under northward $\mathbf{B_Z}$ conditions. Then, dayside reconnection had been turned down and off by northward $\mathbf{B_Z}$, but the SAPS **E** field persisted because of the still existing ring current pressure gradients [*Foster and Burke*, 2002]. As the regular two-cell pattern became distorted or turned into a multicell pattern during northward $\mathbf{B_Z}$ [*Huang et al.*, 2001], the SED plume plasma could not enter the polar cap under such convection conditions, and therefore, the polar cap became a low plasma density region. Based on the V_Y patterns observed, these SAPS-WS events appeared to be the manifestations of Alfven waves [*Mishin and Burke*, 2005]. According to our analysis (see section 4.2), mainly tail connections prevailed under northward $\mathbf{B_Z}$ conditions (see Figure 7) when Alfven waves tend to develop [*Keiling*, 2009]. In fact, Alfven waves act as energy carriers transporting significant amount of energy from the magnetotail to the ionosphere during the release of stored magnetospheric energy at times of substorm expansions [*Keiling*, 2009].

Next, we discuss the mechanism of trough development and the impact of SAPS-WS on the trough. Our results show that both, trough and SAPS-WS, varied during these scenarios. Regarding the mechanism of trough development, the trough developed during the first SAPS-WS event in the initial phase under southward $\mathbf{B_Z}$ conditions. Trough development then was due to flow stagnations, and the trough became further deepened by both R2 FAC-related frictional heating and strong SAPS-related plasma drifts [*Foster and Vo*, 2002]. Meanwhile, the trough became also structured by the underlying SAPS-WS. During the following three main phase SAPS-WS events under northward $\mathbf{B_Z}$ conditions, there was no flow stagnation. As such, the trough developed due to R2 FAC and SAPS **E** field-related processes and became also structured by the underlying SAPS-WS. Although the trough bottom became structured during all four SAPS-WS events, there were differences. Since the stagnation trough was the deepest ($2 \times 10^3\ i^+/\mathrm{cm}^3$; see Figure 2c), its underlying structured SAPS **E** was the strongest ($V_Y \approx 2800$ m/s) due to the feedback mechanisms accelerated by low plasma densities and reduced conductivity [*Mishin et al.*, 2003]. As the following three main phase scenarios reveal, a shallower trough (e.g., $10 \times 10^3\ i^+/\mathrm{cm}^3$; see Figure 3c) was accompanied by a structured but weaker SAPS **E** field ($V_Y \approx 2000$ m/s; see Figure 3c). Furthermore, these main phase scenarios demonstrate also that auroral undulations caused SAPS-WS. Both, the auroral sunward drift occurring in the structured oval region (marked as 1) and the trough poleward region created by solar-produced plasma, became all structured additionally to the trough bottom.

Another interesting feature is the response of SAPS to the auroral undulations taking place in the unstructured oval region (marked as 2; see Figures 4c and 5c). This is demonstrated with two main phase SAPS-WS events, during which auroral oval processes interacted with SAPS. Some earlier moderate auroral undulations triggered the development of less intensive SAPS-WS (see Figure 4c). These became more intensive later on (see Figure 5c). We note here that these SAPS-WS scenarios, shown in Figures 4c and 5c, occurred during the last two ε subpeaks (2500 and 3500 GW, respectively) when the energy input efficiency was increasing (from 0.25 to 0.32 %) during the main phase. We note also that these low % values are in good agreement with the recent statistical results of *Li et al.* [2012]. According to the interpretation of *Henderson et al.* [2010], invoking the work of *Sazykin et al.* [2002], equator moving auroral streamers are produced by patchy or intermittent reconnections in the magnetotail. As our results suggest (see details below), such intermittent magnetotail reconnections occurred during the main phase and was controlled by the efficiency of energy transfer from the solar wind to the magnetosphere. Like the last scenario (see Figure 5c) demonstrates, a more efficient energy transfer and a more intense tail reconnection produced more intensive auroral streamers.

Regarding the underlying energetics, it is possible that some dayside reconnection could also occur during northward $\mathbf{B_Z}$. The reason is that the coupled magnetosphere-ionosphere remains highly dynamic after $\mathbf{B_Z}$ turns northward, and it takes several hours to turn down and later on to turn off dayside reconnection

[*Wygant et al.*, 1983]. However, while polar convection gradually decreased (indicated by the decrease of modeled cross PCP drop (Φ_{PC}) from ~400 to ~100 kV) and remained minimum (Φ_{PC} <100 kV; see Figure 7b), tail connection was the only channel of active energy input during northward $\mathbf{B_Z}$. Then, energetic particles become injected earthward as plasma jets originating from plasmoids (i.e., a body of plasma situated in a closed field line region [*Hones*, 1984]) and traveling across the tail [*Mishin*, 2013]. Further evidence is provided by the ΣE_Y time series (see Figure 7e) showing a plateau and thus indicating that solar energy input paused while $\mathbf{B_Z}$ was northward. But the positive gradient of the Σ*SYM-H* line plot (see Figure 7f) indicates that there was an ongoing energy input into the ring current from 2000 UT onward. By providing direct evidence of reoccurring tail connections with the SAPS-WS scenarios presented, our results add to the recent study of *Du et al.* [2008] on this storm. In their interpretation, a lengthy storage of solar wind energy during northward $\mathbf{B_Z}$ in the magnetotail, and its delayed release into the ring current was a strong possibility supported by their evidence, while the option of substantial magnetic reconnection was also considered.

6. Conclusions

In this study we have focused on the development of structured subauroral polarization streams (SAPS) appearing as SAPS wave structures (WS). The nature of 21–22 January 2005 geomagnetic storm, characterized by two sudden commencements and three main phases, provided a unique opportunity. We have observed various SAPS-WS features, their impact on the midlatitude trough, and the response of subauroral region to auroral processes (e.g., auroral undulations) on the first storm day, 21 January. Our results show that since this storm started under southward $\mathbf{B_Z}$ conditions ($\mathbf{B_Z} < 0$) and unfolded during northward $\mathbf{B_Z}$ ($\mathbf{B_Z} > 0$), dayside reconnection were followed by tail connections. During the initial phase ($\mathbf{B_Z} < 0$), SED plume development was intensive and provided favorable conditions for EMIC wave generation. Then, the SAPS-WS observed was due to the combination of standing (toroid) Alfven waves and EMIC waves and further deepened the midlatitude trough that was a stagnation trough. During the main phase ($\mathbf{B_Z} > 0$), SED development continued but the SED plume was absent in the polar cap leaving it a low plasma density region. During tail connections, each SAPS-WS observed was generated by Alfvenic waves that also acted as carriers of stored energy from the magnetotail to the ionosphere. While the SAPS **E** field and related drift created the main mechanism of trough development, as there was no flow stagnation, the SAPS-WS impacted the shallow trough bottom and the poleward trough region as well. When auroral convections became structured in the structured auroral zone and auroral undulations occurred in the unstructured auroral zone, SAPS-WS developed as a response. Based on the analysis of the four SAPS-WS events presented, the new findings shown in this study are as follows. (1) Stagnation trough promoted stronger SAPS **E** field development and enhanced the impact of SAPS-WS on the trough itself. (2) SAPS-WS impacted not only the entire trough bottom but the trough's solar-produced poleward region as well and thus produced not only steep plasma density gradients but increased plasma densities as well. (3) Undulating sunward auroral drifts both in the structured auroral zone and in the unstructured auroral zone lead to SAPS-WS development demonstrating a strong driver-response relationship. Finally, we note that these new results are significant as they contribute to the better understanding of the various physical processes that control and influence the subauroral and auroral regions and therefore lead to the development of SAPS-WS.

Acknowledgments
This material is based on research sponsored by the Air Force Research Laboratory, under agreement FA2386-15-1-4043. The U.S. Government is authorized to reproduce and distribute reprints for governmental purposes notwithstanding any copyright notation thereon. We are grateful to the ACE SWEPAM instrument team, the ACE Science Center for providing the ACE data. We gratefully acknowledge the Center for Space Sciences at the University of Texas at Dallas and the U.S. Air Force for providing the DMSP thermal plasma data. The DMSP particle detectors were designed by Dave Hardy of AFRL, and data obtained from JHU/APL. Special thanks are extended to MIT for the GPS TEC data in the Madrigal Database and to the Community Coordinated Modeling Center at NASA Goddard Space Flight Center for the TIE-GCM and CTIPe model simulations. Simulation results have been provided by the Community Coordinated Modeling Center through their public Runs on Request system (http://ccmc.gsfc.nasa.gov). The CCMC is a multiagency partnership between NASA, AFMC, AFOSR, AFRL, AFWA, NOAA, NSF, and ONR. The CTIPe model was developed by T. Fuller-Rowell at the Space Environment Center (NOAA SEC). TIE-GCM was developed by Roble et al. at the High Altitude Observatory (HAO), National Center for Atmospheric Research (NCAR). We also thank the World Data Center for Geomagnetism at Kyoto (http://wdc.kugi.kyoto-u.ac.jp/wdc/Sec3.html) for providing the geomagnetic data and indices, and the Space Physics Interactive Data Resource (SPIDR) for the magnetic data (http://spidr.ngdc.noaa.gov/spidr/dataset.do?view=geomagnetic).

References

Akasofu, S.-I. (1981), Energy coupling between the solar wind and the magnetosphere, *Space Sci. Rev.*, *28*, 121–190, doi:10.1007/BF00218810.

Anderson, P. C., W. B. Hanson, R. A. Heelis, J. D. Craven, D. N. Baker, and L. A. Frank (1993), A proposed production model of rapid subauroral ion drifts and their relationship to substorm evolution, *J. Geophys. Res.*, *98*(A4), 6069–6078, doi:10.1029/92JA01975.

Anderson, P. C., D. L. Carpenter, K. Tsuruda, T. Mukai, and F. J. Rich (2001), Multisatellite observations of rapid subauroral ion drifts (SAID), *J. Geophys. Res.*, *106*(A12), 29,585–29,599, doi:10.1029/2001JA000128.

Brinton, H. C., J. M. Grebowsky, and L. H. Brace (1978), The high-latitude winter *F* region at 300 km: Thermal plasma observations from AE-C, *J. Geophys. Res.*, *83*, 4767–4776, doi:10.1029/JA083iA10p04767.

Chen, L., R. M. Thorne, and R. B. Horne (2009), Simulation of EMIC wave excitation in a model magnetosphere including structured high-density plumes, *J. Geophys. Res.*, *114*, A07221, doi:10.1029/2009JA014204.

Du, A. M., B. T. Tsurutani, and W. Sun (2008), Anomalous geomagnetic storm of 21–22 January 2005: A storm main phase during northward IMFs, *J. Geophys. Res.*, *113*, A10214, doi:10.1029/2008JA013284.

Du, A. M., B. T. Tsurutani, and W. Sun (2012), Comments on "Interplanetary and geomagnetic parameters during January 16–26, 2005" by R. P. Kane, *Planet. Space Sci.*, *71*(1), 55–56, doi:10.1016/j.pss.2012.07.002.

Erickson, P. J., J. C. Foster, and J. M. Holt (2002), Inferred electric field variability in the polarization jet from Millstone Hill E region coherent scatter observations, *Radio Sci.*, *37*(2), 1027, doi:10.1029/2000RS002531.

Foster, J. C. (1993), Storm time plasma transport at middle and high latitudes, *J. Geophys. Res.*, *98*(A2), 1675–1689, doi:10.1029/92JA02032.

Foster, J. C., and H. B. Vo (2002), Average characteristics and activity dependence of the subauroral polarization stream, *J. Geophys. Res.*, *107*(A12), 1475, doi:10.1029/2002JA009409.

Foster, J. C., and W. J. Burke (2002), SAPS: A new characterization for sub-auroral electric fields, *Eos Trans. AGU*, *83*, 393, doi:10.1029/2002EO000289.

Foster, J. C., M. J. Buonsanto, M. Mendillo, D. Nottingham, F. J. Rich, and W. Denig (1994), Coordinated stable auroral red arc observations: Relationship to plasma convection, *J. Geophys. Res.*, *99*(A6), 11,429–11,439, doi:10.1029/93JA03140.

Foster, J. C., P. J. Erickson, A. J. Coster, J. Goldstein, and F. J. Rich (2002), Ionospheric signatures of plasmaspheric tails, *Geophys. Res. Lett.*, *29*(13), 1623, doi:10.1029/2002GL015067.

Foster, J. C., A. J. Coster, P. J. Erickson, F. J. Rich, and B. R. Sandel (2004), Stormtime observations of the flux of plasmaspheric ions to the dayside cusp/magnetopause, *Geophys. Res. Lett.*, *31*, L08809, doi:10.1029/2004GL020082.

Foster, J. C., A. J. Coster, P. J. Erickson, J. M. Holt, F. D. Lind, W. Rideout, M. McCready, A. van Eyken, R. J. Barnes, R. A. Greenwald, and F. J. Rich (2005), Multiradar observations of the polar tongue of ionization, *J. Geophys. Res.*, *110*, A09S31, doi:10.1029/2004JA010928.

Fraser, B. J., and T. S. Nguyen (2001), Is the plasmapause a preferred source region of electromagnetic ion cyclotron waves in the magnetosphere?, *J. Atmos. Sol. Terr. Phys.*, *63*, 1225–1247, doi:10.1016/S1364-6826(00)00225-X.

Fuller-Rowell, T. J., G. H. Millward, A. D. Richmond, and M. V. Codrescu (2002), Storm-time changes in the upper atmosphere at low latitudes, *J. Atmos. Sol. Terr. Phys.*, *64*(12–14), 1383–1391, doi:10.1016/S1364-6826(02)00101-3.

Galperin, Y., V. N. Ponomarev, and A. G. Zosimova (1974), Plasma convection in the polar ionosphere, *Ann. Geophys.*, *30*(1), 1–7.

Henderson, M. G., E. F. Donovan, J. C. Foster, I. R. Mann, T. J. Immel, S. B. Mende, and J. B. Sigwarth (2010), Start-to-end global imaging of a sunward propagating, SAPS-associated giant undulation event, *J. Geophys. Res.*, *115*, A04210, doi:10.1029/2009JA014106.

Hones, E. W. (1984), Plasma sheet behavior during substorms, in *Magnetic Reconnection in Space and Laboratory Plasmas*, edited by E. W. Hones, AGU, Washington, D. C., doi:10.1029/GM030p0178.

Huang, C.-S., J. C. Foster, and J. M. Holt (2001), Westward plasma drift in the midlatitude ionospheric *F* region in the midnight-dawn sector, *J. Geophys. Res.*, *106*(A12), 30,349–30,362, doi:10.1029/2001JA001110.

Huang, C.-S., J. Foster, L. Goncharenko, G. Reeves, J. Chau, K. Yumoto, and K. Kitamura (2004), Variations of low-latitude geomagnetic fields and *Dst* index caused by magnetic substorms, *J. Geophys. Res.*, *109*, A05219, doi:10.1029/2003JA010334.

Huang, Y., C. Y. Huang, Y.-J. Su, Y. Deng, and X. Fang (2014), Ionization due to electron and proton precipitation during the August 2011 storm, *J. Geophys. Res. Space Physics*, *119*, 3106–3116, doi:10.1002/2013JA019671.

Jordanova, V. K., M. Spasojević, and M. F. Thomsen (2007), Modeling the electromagnetic ion cyclotron wave-induced information of detached subauroral proton arcs, *J. Geophys. Res.*, *112*, A08209, doi:10.1029/2006JA012215.

Kalegaev, V., N. A. Vlasova, and Z. Peng (2015), Dynamics of the magnetosphere during geomagnetic storms on January 21–22, 2005 and December 14–15, 2006, *Cosmic Res.*, *53*(2), 98–110, doi:10.1134/S0010952515020033.

Keiling, A. (2009), Alfvén waves and their roles in the dynamics of the Earth's magnetotail: A review, *Space Sci. Rev.*, *142*(1–4), 73–156, doi:10.1007/s11214-008-9463-8.

Kelley, M. C. (1986), Intense sheared flow as the origin of large-scale undulations of the edge of the diffuse aurora, *J. Geophys. Res.*, *91*(A3), 3225–3230, doi:10.1029/JA091iA03p03225.

Keskinen, M. J., S. Basu, and S. Basu (2004), Midlatitude subauroral small scale structure during a magnetic storm, *Geophys. Res. Lett.*, *31*, L09811, doi:10.1029/2003GL019368.

Knudsen, W. C. (1974), Magnetospheric convection and the high-latitude F_2 ionosphere, *J. Geophys. Res.*, *79*, 1046–1055, doi:10.1029/JA079i007p01046.

Kozyra, J. U., et al. (1987), Satellite observations of new particle and field signatures associated with SAR arc field lines at magnetospheric heights, *Adv. Space Res.*, *7*(8), 3–6, doi:10.1016/0273-1177(87)90181-5.

LaBelle, J., and R. A. Treumann (1988), Plasma waves at the dayside magnetopause, *Space Sci. Rev.*, *47*(1), 175–202, doi:10.1007/BF00223240.

Lee, I. T., W. Wang, J. Y. Liu, C. Y. Chen, and C. H. Lin (2011), The ionospheric midlatitude trough observed by FORMOSAT-3/COSMIC during solar minimum, *J. Geophys. Res.*, *116*, A06311, doi:10.1029/2010JA015544.

Li, H., C. Wang, W. Y. Xu, and J. R. Kan (2012), Characteristics of magnetospheric energetics during geomagnetic storms, *J. Geophys. Res.*, *117*, A04225, doi:10.1029/2012JA017584.

Mannucci, A. J., B. T. Tsurutani, B. A. Iijima, A. Komjathy, A. Saito, W. D. Gonzalez, F. L. Guarnieri, J. U. Kozyra, and A. Skoug (2005), Dayside global ionospheric response to the major interplanetary events of October 29–30, 2003 "Halloween Storms", *Geophys. Res. Lett.*, *32*, L12S02, doi:10.1029/2004GL021467.

Mishin, E., and Blaunstein, N. (2008), Irregularities within subauroral polarization stream-related troughs and GPS radio interference at midlatitudes, in *Midlatitude Ionospheric Dynamics and Disturbances*, edited by P. M. Kintner, et al., AGU, Washington, D. C., doi:10.1029/181GM26.

Mishin, E. V. (2013), Interaction of substorm injections with the subauroral geospace: 1. Multispacecraft observations of SAID, *J. Geophys. Res. Space Physics*, *118*, 5782–5796, doi:10.1002/jgra.50548.

Mishin, E. V., and V. M. Mishin (2007), Prompt response of SAPS to stormtime substorms, *J. Atmos. Sol. Terr. Phys.*, *69*, 1233–1240, doi:10.1016/j.jastp.2006.09.009.

Mishin, E. V., and W. J. Burke (2005), Stormtime coupling of the ring current, plasmasphere, and topside ionosphere: Electromagnetic and plasma disturbances, *J. Geophys. Res.*, *110*, A07209, doi:10.1029/2005JA011021.

Mishin, E. V., W. J. Burke, C. Y. Huang, and F. J. Rich (2003), Electromagnetic wave structures within subauroral polarization streams, *J. Geophys. Res.*, *108*(A8), 1309, doi:10.1029/2002JA009793.

Mishin, E., J. Foster, A. Potekhin, F. Rich, K. Schlegel, K. Yumoto, V. Taran, J. Ruohoniemi, and R. Friedel (2002), Global ULF disturbances during a stormtime substorm on 25 September 1998, *J. Geophys. Res.*, *107*(A12), 1486, doi:10.1029/2002JA009302.

Mishin, E., W. Burke, and A. Viggiano (2004), Stormtime subauroral density troughs: Ion-molecule kinetics effects, *J. Geophys. Res.*, *109*, A10301, doi:10.1029/2004JA010438.

Moffett, R. J., and S. Quegan (1983), The mid-latitude trough in the electron concentration of the ionospheric *F*-layer: A review of observations and modeling, *J. Atmos. Terr. Phys.*, *45*, 315–343, doi:10.1016/S00219169(83)80038-5.

Morley, S. K., S. T. Ables, M. D. Sciffer, and B. J. Fraser (2009), Multipoint observations of Pc1-2 waves in the afternoon sector, *J. Geophys. Res.*, *114*, A09205, doi:10.1029/2009JA014162.

Muldrew, D. B. (1965), *F*-layer ionization trough deduced from Alouette data, *J. Geophys. Res.*, *70*, 2635–2650, doi:10.1029/JZ070i011p02635.

Newell, P. T., Y. I. Feldstein, Y. I. Galperin, and C.-I. Meng (1996), Morphology of nightside precipitation, *J. Geophys. Res.*, *101*(A5), 10,737–10,748, doi:10.1029/95JA03516.

Perreault, W. K., and S.-I. Akasofu (1978), A study of geomagnetic storms, *Geophys. J. R. Astron. Soc.*, *54*, 547–573, doi:10.1111/j.1365-246X.1978.tb05494.

Petrinec, S. M., and C. T. Russell (1996), Near-Earth magnetotail shape and size as determined from the magnetopause flaring angle, *J. Geophys. Res.*, *101*(A1), 137–152, doi:10.1029/95JA02834.

Prolss, G. W. (2006), Subauroral electron temperature enhancement in the nighttime ionosphere, *Ann. Geophys.*, *24*(7), 1871–1885, doi:10.5194/angeo-24-1871-2006.

Richmond, A. D., E. C. Ridley, and R. G. Roble (1992), A thermosphere/ ionosphere general circulation model with coupled electrodynamics, *Geophys. Res. Lett.*, *19*, 601–604, doi:10.1029/92GL00401.

Rodger, A. S., R. J. Moffett, and S. Quegan (1992), The role of ion drift in the formation of ionization troughs in the mid- and high-latitude ionosphere—A review, *J. Atmos. Terr. Phys.*, *54*, 1–30, doi:10.1016/0021-9169(92)90082-V.

Sandholt, P. E., C. J. Farrugia, and W. F. Denig (2014), M–I coupling across the auroral oval at dusk and midnight: Repetitive substorm activity driven by interplanetary coronal mass ejections (CMEs), *Ann. Geophys.*, *32*, 333–351, doi:10.5194/angeo-32-333-2014.

Sazykin, S., R. A. Wolf, R. W. Spiro, T. I. Gombosi, D. L. De Zeeuw, and M. F. Thomsen (2002), Interchange instability in the inner magnetosphere associated with geosynchronous particle flux decreases, *Geophys. Res. Lett.*, *29*(10), doi:10.1029/2001GL014416.

Schunk, R. W., P. M. Banks, and W. J. Raitt (1976), Effects of electric fields and other processes upon the nighttime high-latitude *F* layer, *J. Geophys. Res.*, *81*, 3271–3282, doi:10.1029/JA081i019p03271.

Shue, J.-H., J. K. Chao, H. C. Fu, C. T. Russell, P. Song, K. K. Khurana, and H. J. Singer (1997), A new functional form to study the solar wind control of the magnetopause size and shape, *J. Geophys. Res.*, *102*(A5), 9497–9511, doi:10.1029/97JA00196.

Sojka, J. J., R. W. Schunk, W. R. Hoegy, and J. M. Grebowsky (1991), Model and observation comparison of the universal time and IMF B_Y dependence of the ionospheric polar hole, *Adv. Space Res.*, *11*(10), 39–42.

Spiro, R. W., R. A. Heelis, and W. B. Hanson (1979), Rapid subauroral ion drifts observed by Atmosphere Explorer C, *Geophys. Res. Lett.*, *6*, 657–660, doi:10.1029/GL006i008p00657.

Stern, D. P. (1975), The motion of a proton in the equatorial magnetosphere, *J. Geophys. Res.*, *80*(4), 595–599, doi:10.1029/JA080i004p00595.

Streltsov, A., and J. Foster (2004), Electrodynamics of the magnetosphere-ionosphere coupling in the nightside subauroral zone, *Phys. Plasmas*, *11*(4), 1260, doi:10.1063/11647139.

Streltsov, A. V., and E. V. Mishin (2003), Numerical modeling of localized electromagnetic waves in the nightside subauroral zone, *J. Geophys. Res.*, *108*(A8), 1332, doi:10.1029/2003JA009858.

Su, Y.-. J., M. F. Thomsen, J. E. Borovsky, and J. C. Foster (2001), A linkage between polar patches and plasmaspheric drainage plumes, *Geophys. Res. Lett.*, *28*, 111–113, doi:10.1029/2000GL012042.

Troshichev, O. A., R. Y. Lukianova, V. O. Papitashvili, F. J. Rich, and O. Rasmussen (2000), Polar cap index (PC) as a proxy for ionospheric electric field in the near-pole region, *Geophys. Res. Lett.*, *27*, 3809–3812, doi:10.1029/2000GL003756.

Troshichev, O., H. Hayakawa, A. Matsuoka, T. Mukai, and K. Tsuruda (1996), Cross polar cap diameter and voltage as a function of PC index and interplanetary quantities, *J. Geophys. Res.*, *101*(A6), 13,429–13,435, doi:10.1029/95JA03672.

Volland, H. (1978), A model of the magnetospheric electric convection field, *J. Geophys. Res.*, *83*(A6), 2695–2699, doi:10.1029/JA083iA06p02695.

Wang, C., J. P. Han, H. Li, Z. Peng, and J. D. Richardson (2014), Solar wind-magnetosphere energy coupling function fitting: Results from a global MHD simulation, *J. Geophys. Res. Space Physics*, *119*, 6199–6212, doi:10.1002/2014JA019834.

Winningham, J. D., and W. J. Heikkila (1974), Polar cap auroral electron fluxes observed with ISIS 1, *J. Geophys. Res.*, *79*, 949–957, doi:10.1029/JA079i007p00949.

Winningham, J. D., W. J. Heikkila, F. Yasuhara, and S.-I. Akasofu (1975), The latitudinal morphology of 10-eV to 10-keV electron fluxes during magnetically quiet and disturbed times in the 2100–0300 MLT sector, *J. Geophys. Res.*, *80*, 3148–3171, doi:10.1029/JA080i022p03148.

Wygant, J. R., R. B. Torbert, and F. S. Mozer (1983), Comparison of S3-3 polar cap potential drops with the interplanetary magnetic field and models of magnetopause reconnection, *J. Geophys. Res.*, *88*(A7), 5727–5735, doi:10.1029/JA088iA07p05727.

Yuan, Z., Y. Xiong, Y. Pang, M. Zhou, X. Deng, J. G. Trotignon, E. Lucek, and J. Wang (2012), Wave-particle interaction in a plasmaspheric plume observed by a Cluster satellite, *J. Geophys. Res.*, *117*, A03205, doi:10.1029/2011JA017152.

Zhang, Q. H., et al. (2013), Direct observations of the evolution of polar cap ionization patches, *Science*, *339*, 1597–1600, doi:10.1123/science/1231487.